diabetes®
American Diabetes Association®

Protective *Renalase* Deficiency in β-Cells Shapes Immune Metabolism and Function in Autoimmune Diabetes

Kevin Bode, Tara MacDonald, Taylor Stewart, Bryhan Mendez, Erica P. Cai, Noelle Morrow, Yu-Chi Lee, Peng Yi, and Stephan Kissler

Diabetes 2023;72(8):1127–1143 | https://doi.org/10.2337/db23-0030

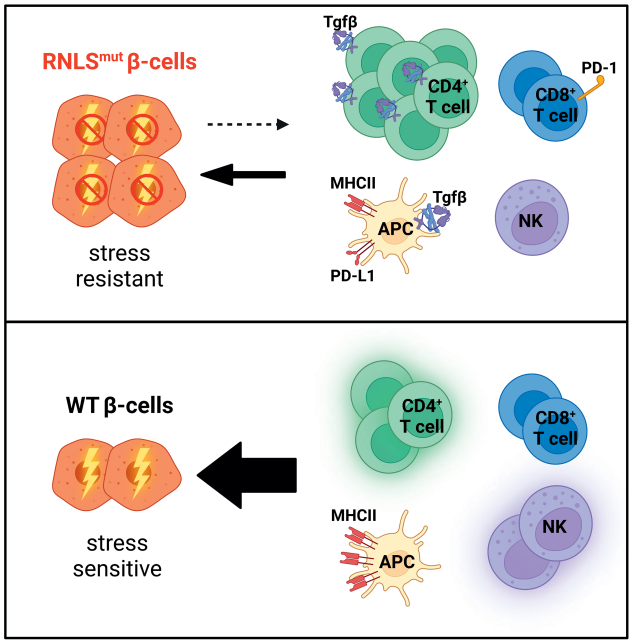

Protective *Renalase* Deficiency in β-Cells Shapes Immune Metabolism and Function in Autoimmune Diabetes

Kevin Bode,[1,2] Tara MacDonald,[1,2] Taylor Stewart,[2,3] Bryhan Mendez,[1] Erica P. Cai,[3] Noelle Morrow,[3] Yu-Chi Lee,[3] Peng Yi,[2,3,4] and Stephan Kissler[1,2,4]

Diabetes 2023;72:1127–1143 | https://doi.org/10.2337/db23-0030

Type 1 diabetes (T1D) is caused by the immune-mediated loss of pancreatic β-cells that produce insulin. The latest advances in stem cell (SC) β-cell differentiation methods have made a cell replacement therapy for T1D feasible. However, recurring autoimmunity would rapidly destroy transplanted SC β-cells. A promising strategy to overcome immune rejection is to genetically engineer SC β-cells. We previously identified *Renalase* (*Rnls*) as a novel target for β-cell protection. Here we show that *Rnls* deletion endows β-cells with the capacity to modulate the metabolism and function of immune cells within the local graft microenvironment. We used flow cytometry and single-cell RNA sequencing to characterize β-cell graft-infiltrating immune cells in a mouse model for T1D. Loss of *Rnls* within transplanted β-cells affected both the composition and the transcriptional profile of infiltrating immune cells in favor of an anti-inflammatory profile with decreased antigen-presenting capacity. We propose that changes in β-cell metabolism mediate local immune regulation and that this feature could be exploited for therapeutic goals.

ARTICLE HIGHLIGHTS

- Protective *Renalase* (*Rnls*) deficiency impacts β-cell metabolism.
- *Rnls*-deficient β-cell grafts do not exclude immune infiltration.
- *Rnls* deficiency in transplanted β-cells broadly modifies local immune function.
- Immune cell in *Rnls* mutant β-cell grafts adopt a non-inflammatory phenotype.

Type 1 diabetes (T1D) is an autoimmune disease that causes the loss of insulin-producing β-cells in the pancreas. Within a year of clinical manifestation, when most β-cell mass has been eliminated by autoimmunity, a curative therapy for T1D must include a β-cell replacement that fully restores a patient's ability to produce insulin (1). The latest advances in the manufacture of stem cell (SC)-derived β-cells have made such a cell replacement therapy a realistic prospect (2). The critical hurdle to implementing this strategy in the clinic remains our inability to protect β-cells against autoimmunity without resorting to broad immunosuppression. Further, current limitations in our ability to generate patient-specific SC β-cells mean that—at least for the foreseeable future—a cellular therapy for T1D will necessitate protection against alloimmunity as well. Using genome-editing tools, several groups have started engineering SCs and SC β-cells to protect them against immune-mediated killing. Most of these efforts so far have centered around the deletion of genes encoding MHC molecules and the addition of known immune inhibitory ligands, including PD-L1 and CD47 (3–6).

Taking, instead, an unbiased approach reliant on genome-wide screening, we previously reported that targeting the gene *Renalase* (*Rnls*) in β-cells afforded significant protection against cell stress-induced apoptosis in vitro and autoimmune killing in vivo (7). *Rnls* function has not yet been

[1]Section for Immunobiology, Joslin Diabetes Center, Boston, MA
[2]Department of Medicine, Harvard Medical School, Boston, MA
[3]Section for Islet Cell and Regenerative Biology, Joslin Diabetes Center, Boston, MA
[4]Diabetes Program, Harvard Stem Cell Institute, Cambridge, MA
Corresponding author: Stephan Kissler, stephankissler@gmail.com

Received 9 January 2023 and accepted 30 April 2023

This article contains supplementary material online at https://doi.org/10.2337/figshare.22898705.

fully elucidated, and the mechanism by which *Rnls* deficiency protects β-cells is not clear. The protein encoded by *Rnls* is predicted to act as a cytosolic oxidase, but neither its physiological substrate nor its product is known (8,9). Our previous research had determined that *Rnls* deletion did not broadly prevent antigen presentation or make cells resistant to all apoptotic stimuli (7). Understanding how the loss of *Rnls* protects β-cells against autoimmunity could help in the search for additional modifications to protect SC β-cells against immune-mediated killing.

We have now determined that *Rnls* deletion broadly modifies β-cell metabolism, causing a marked increase in glycolysis. We speculated that a metabolic shift could have two non–mutually exclusive outcomes that may explain the protective effect of *Rnls* deletion in β-cells. First, cellular metabolism is known to intersect with stress pathways (10–12), suggesting that favorable metabolic changes could improve cell-intrinsic stress resistance. Second, cellular metabolism can impact the extracellular microenvironment and modulate local immune function. This is best exemplified by cancer cell metabolites implicated in local immune suppression in the tumor microenvironment (13–16). We hypothesized that a change in β-cell metabolism could similarly modify the functionality of immune cells involved in β-cell autoimmunity. To explore this notion, we utilized an experimental model of β-cell transplantation where grafts are rapidly infiltrated and destroyed by immune cells in a pathophysiological process replicating recurring autoimmunity (7). We found that the protective deletion of *Rnls* in grafted β-cells had only a modest effect on the overall composition of immune infiltrates. However, *Rnls* mutant β-cells induced a significant change in the transcriptional program of immune cells that displayed a shift in metabolic pathways and features of cellular starvation accompanied with expression of hallmark anti-inflammatory genes.

RESEARCH DESIGN AND METHODS

Cell Lines and Generation of *Rnls* Mutant and PD-L1–Overexpressing NIT-1 Cells

NIT-1 and 293FT cell lines were obtained from ATCC (catalog no. CRL-2055) and Thermo Fisher Scientific (catalog no. R70007), respectively. Cells were maintained in DMEM, high glucose, pyruvate (catalog no. 11-995-073; Gibco), supplemented with 10% FCS (catalog no. 10-082-147; Gibco), 50 μmol/L 2-Mercaptoethanol (catalog no. 60-24-2; Sigma-Aldrich), and penicillin/streptomycin (catalog no. 15140122; Thermo Fisher Scientific) in a 37°C incubator with 5% CO_2. *Rnls* mutant or nontarget (NT, referred to as wild-type [WT] throughout) NIT-1 cells were generated as previously described (7). In brief, NT guide RNA [gRNA] (5′-TAAAAACGCTGGCGG CCTAG-3′, MGLibA_67395) and *Rnls* gRNA (5′-CTACTCCTC TCGCTATGCTC-3′, MGLibA_46009) were cloned into lenti-CRISPR v.2 vector. Lentivirus containing NT or *Rnls* gRNA was used to establish these respective cell lines. The *Rnls* mutation was confirmed by deep-sequencing analysis(Massachusetts General Hospital DNA Core Facility) and quantitative PCR (data not shown). PD-L1–overexpressing NIT-1 cell lines were generated by lentiviral transduction of WT or *Rnls* mutant NIT-1 cells with CMV promoter-driven full-length mouse PD-L1 (plenti-PDL1-DEST; Addgene). Following Blasticidin S HCl (catalog no. A1113903; Thermo Fisher Scientific) selection for 7 days, cells were stained for PD-L1 (catalog no. 124334; Biolegend) and FACS sorted to select only PD-L1^{high}–expressing cells.

Bulk RNA Sequencing

For bulk RNA sequencing (RNAseq) analysis, triplicates of 2×10^6 WT and *Rnls* mutant NIT-1 cells were used for RNA isolation using Zymo Quick-RNA miniprep plus kit (catalog no. R1058; Zymo Research), following the manufacturer's protocol. RNA libraries were prepared, and were subsequently quality control tested by Novogene Corporation Inc. Sequencing was performed on an Illumina NovaSeq 6000 sequencing system for >20 million read data output (Novogen Corporation Inc.). For reactome enrichment analysis, the 500 most upregulated genes in *Rnls* mutant versus WT control were used.

Seahorse Metabolic Flux Assay

On the day prior to the experiment, WT or *Rnls* mutant NIT-1 cells were seeded at 1.2×10^5 cells per well on a 96-well plate in Agilent XF DMEM pH 7.4 media (catalog no. 103575-100; Agilent), supplemented with 1 mmol/L pyruvate, 2 mmol/L glutamine, and 10 mmol/L glucose (XF DMEM media). After seeding, the plate rested for 1 h at 37°C in the absence of CO_2 and was then placed in a standard 37°C cell incubator overnight. The following morning, cell health, morphology, and uniformity were confirmed by microscopy. Cells were washed three times with XF DMEM media and replaced with fresh XF DMEM to a final volume of 180 μL. The real-time flux of both H^+ production (extracellular acidification rate [ECAR]; mpH/min) and O_2 consumption (OCR; pmol/min) were measured simultaneously every 6 min for the duration of the assay.

Flow Cytometry

All staining procedures were performed in PBS/10% FCS. Single-cell suspensions were preincubated with Fc-block antibody (catalog no. 156604; Biolegend) for 5 min, then stained with antibodies against indicated cell surface molecules (Table 1) for 20 min on ice. Appropriate isotype controls were purchased from Biolegend. Dead cells were excluded using Propidium Iodide (PI, catalog no. R37169; Thermo Fisher Scientific) or fixable viability dye eFluor 450 (catalog no. 65-0863; eBiosciences). For PD-L1 induction, 5×10^5 NIT-1 cells (WT or Rnls^{mut}) were seeded in six-well plates and incubated for 24 h with the indicated concentration of recombinant mouse IFN-γ (catalog no. 575306; Biolegend) before PD-L1 surface staining. Data were acquired on an LSRII instrument (BD Biosciences) and analyzed with FlowJo software v.10.6.1 (FlowJo LLC). All data are shown using log-scale axes. A list of antibodies used for flow cytometry is included in Table 1.

Table 1—Antibodies used for flow cytometry

Antibody	Clone	Catalog no.	Vendor
CD3 Brilliant Violet 785	17A2	100232	Biolegend
CD4 APC	RM4-5	100516	Biolegend
CD8 FITC	53-6.7	100706	Biolegend
CD11b APC-Cy7	M1/70	101226	Biolegend
CD11c Brilliant Violet 711	N418	117349	Biolegend
CD19 Pacific Blue	1D3/CD19	152416	Biolegend
CD25 Pacific Blue	PC61	102022	Biolegend
CD44 APC-Cy7	IM7	103028	Biolegend
CD45 PE-Cy7	30-F11	103114	Biolegend
CD45RB PE	C363-16A	103308	Biolegend
CD69 PE-Cy5	H1.2F3	104510	Biolegend
CD152 (CTLA4) Brilliant Violet 421	UC10-4B9	106312	Biolegend
F4/80 FITC	BM8	123108	Biolegend
I-A^k (MHC class II) PE	10-3.6	109908	Biolegend
LAP (TGF-β1) PE	TW7-16B4	141404	Biolegend
Ly-6C Brilliant Violet 421	HK1.4	128032	Biolegend
Ly-6G Brilliant Violet 785	1A8	127645	Biolegend
NKp46 PerCP/Cyanine5.5	29A1.4	137610	Biolegend
PD-1 Brilliant Violet 711	29F.1A12	135231	Biolegend
PD-L1 PerCP/Cyanine5.5	10F.9G2	124334	Biolegend

$CD4^+$ T-Cell Proliferation Assay

$CD25^-CD4^+$ T cells were obtained from 7- to 10-wk-old nondiabetic NOD mice using a $CD4^+CD25^+$ T Cell Isolation Kit (catalog no. 130-091-041; Miltenyi Biotec). NIT-1 cells were seeded in each well of a 96-well flat-bottom plate in 100 μL T-cell assay medium (RPMI 1640 with 10% FCS, 50 μmol/L 2-Mercaptoethanol, 1 mmol/L sodium pyruvate, 25 mmol/L HEPES buffer and penicillin/streptomycin) following incubation for 5 h in a 37°C incubator with 5% CO_2. $CD25^-CD4^+$ T cells were fluorescently labeled using Tag-it Violet proliferation dye according to the manufacturers' protocol (catalog no. 425101; Biolegend), and 50,000 T cells were added to NIT-1 cell–containing 96-well plates either in direct coculture or on a transwell insert (catalog no. 3380; Corning). Dynabeads Mouse T-Activator (catalog no. 11452D; Thermo Fisher Scientific) (40,000 per well) was added to stimulate T cells. Cells were cocultured in a 37°C incubator with 5% CO_2 for 72 h, then collected and stained with CD45 PE-Cy 7, CD3 Brilliant Violet 785, and CD4 allophycocyanin (APC) antibodies. PI viability dye was used for dead cell staining, flow cytometry was performed on an LSR II instrument (BD Biosciences), and data were analyzed using FlowJo v.10.6.1 (FlowJo LLC).

In Vivo Splenocyte Transfer Mouse Model

NIT-1 WT and *Rnls* mutant (or nontransduced NIT-1 cells and PD-L1–overexpressing NIT-1 cells of the indicated genotypes) (1.5×10^7 each) were injected subcutaneously into opposite flanks of immunodeficient NOD.scid mice. For ex vivo analysis of PD-L1 surface expression in NIT-1 cells, the cells were labeled with carboxy-fluoroscein succinimidyl ester (CFSE, catalog no. 423801; BioLegend) according to manufacturers' instruction prior to implantation. Four days later, autoreactive splenocytes from recently diabetic NOD mice were isolated, and red blood cells were lysed using 5 mL Ammonium-Chloride-Potassium (ACK) lysing buffer (catalog no. A1049201; Thermo Fisher Scientific) for 4 min at room temperature. Lysis was stopped using 5 mL PBS/10% FCS followed by two washing steps using PBS only. Splenocytes were filtered two times, in total, through a strainer with 70-μm pore size to obtain a single-cell solution for counting. Splenocytes (1×10^7) were injected intravenously (i.v.) into NIT-1 cell-bearing NOD.scid mice to transfer autoimmune β-cell killing for up to 23 days. In some experiments, antibodies of indicated amounts against PD-L1 (catalog no. BE0101; Bio X Cell) (refer to Fig. 7*A*) or nontargeting control antibody (catalog no. 14-4616-82; eBioscience) were administered intraperitoneally or subcutaneously in close proximity to the grafts at indicated time points.

Graft Isolation and Single-Cell Preparation

NIT-1 β-cell grafts were isolated and scaled on an analytical balance at indicated time points. Grafts were cut into small

pieces and digested using HEPES buffered RPMI 1640 (catalog no. R4130-10L; Sigma-Aldrich) supplemented with 1 mg/mL Collagenase D (catalog no. 11088858001; Sigma-Aldrich), 20 μg/mL DNase I (catalog no. EN0521; Thermo Fisher Scientific), 2% FCS, and 50 μg/mL lipopolysaccharide neutralizing agent Polymyxin B sulfate (catalog no. 1405-20-5; Sigma-Aldrich) for 45 min at 37°C while shaking at maximum speed on a heating block. Digested grafts were further disaggregated and filtered through a strainer with 70-μm pore size two times to obtain a single-cell solution. For flow cytometry analysis, cells were stained with the antibodies listed in Table 1 in two separate panels (panel 1: T cells and NK cells; panel 2: myeloid cells and B cells). For single-cell RNAseq (scRNAseq) analysis, cells were stained with anti-CD45 and PI in combination with one of four TotalSeq anti-mouse Hashtag antibodies (A0301, A0302, A0303, or A0304) (catalog no. 15580-1/3/5/7, clones M1/42 and 30-F11; Biolegend) to distinguish immune cells derived from individual NIT-1 β-cell grafts.

scRNAseq

WT or *Rnls* mutant graft-infiltrating immune cells were FACS sorted ($CD45^+$ PI^-). Individual samples were labeled using hashtag antibodies, and scRNAseq was performed on pooled samples using the Chromium Next GEM Single Cell 3' GEM, Library & Gel Bead Kit v3.1 (catalog no. PN-1000213; 10× Genomics) according to manufacturer's instructions. Samples were superloaded with 40,000 cells per reaction. The hashtag oligo library (HTO) was generated separately as described previously (https://citeseq.files.wordpress.com/2019/02/cell_hashing_protocol_190213.pdf). Illumina NovaSeq 6000 with approximately 1.1 billion reads was used to sequence the gene expression library, while the HTO library was sequenced separately by Illumina NextSeq with about 130 million reads total each. Gene unique molecular identifier (UMI) counts and hashtag counts in droplets were generated by aligning reads to the mouse genome (mm10) using the multi function of cellranger (17). To distinguish between droplets containing cell RNA and ambient RNA, Monte Carlo simulations were used to compute *P* values for the multinomial sampling transcripts from the ambient pool (18). Barcodes were assumed to correspond to empty droplets if their total UMI counts were at or below 50, and cells were called at a false discovery rate (FDR) of 0.1%. The number of Monte Carlo iterations determined the lower bound for the *P* values (19). The maximum contribution of the ambient solution to the expression profile was computed for cell-containing droplets (18). First, the composition of the ambient pool of RNA was estimated based on the barcodes with total UMI counts less than or equal to 50. Second, the mean ambient contribution for each gene was computed by scaling the ambient pool by some factor. Third, a *P* value for each gene was computed based on the probability of observing an ambient count equal to or below that in cell-containing droplets based on Poisson distribution. Fourth, *P* values across all genes were combined using Simes method (20). This was performed for a range of scaling factors to identify the largest factor that yields a combined *P* value above threshold 0.1, so that the ambient proportions were the maximum estimations. Principal component analysis was performed on the transformed data. Only the top 3,000 variable genes were used as input. A *K*-nearest neighbor network of the cells was constructed based on the Euclidean distance in the space defined by the top principal components that were selected by Horn's parallel analysis (21). The weights of the connection between pairs of cells were refined based on their shared overlap in their local neighborhoods, that is, Jaccard (22). To cluster the cells, modularity optimization techniques, that is, the Louvain algorithm (23), was applied. Ambient RNA contamination was removed from the cluster-level profiles, and the effect of those changes was propagated back to the individual cells using the removeAmbience function of the R package DropletUtils (18). Cells were demultiplexed into four replicated samples base on HTOs (24). Briefly, a *k*-medoid clustering was performed on the normalized HTO values, which initially separated cells into *K*(number of samples) + 1 clusters. A "negative" distribution for HTO was then calculated. For each HTO, the cluster with the lowest average value was used as the negative group, and a negative binomial distribution was fitted to the negative cluster. The 0.99 quantile of this distribution was used as a threshold. Based on these thresholds, each cell was classified as positive or negative for each HTO. Cells that were positive for more than one HTO were annotated as HTO doublets. Doublets (i.e., droplets that had more than one cell with the same HTO) were identified using the R package scDblFinder (25) and removed from the downstream analysis. All the samples of the four replicates were combined, including genes that were detected in at least one cell and including cells where at least one gene was detected. Quality control metrics were used to filter cells that had less than 1,000 UMI (low-quality cells), less than 500 features (low-quality cells), and more than 10% mitochondrial UMI (dying cells). The combined data were normalized using the R package sctransform (26). For cell cluster assignment, markers were found for every cluster compared with all remaining cells using the Wilcoxon rank-sum test, and only markers with a log2FC threshold greater than 0.25 and expressed in more than 10% of the cells were reported. For cell type identification, an automatic tool, Cluster Indentity PRedictor (CIPR) (27), was used to annotate cell types with the reference from Immunological Genome Project (ImmGen). For differential gene expression (DGE) between genotypes and cell types, the gene counts were aggregated for each cell type in each sample. To filter out low-expressing genes, genes were kept that had counts per million more than one in at least four samples of a cell type; 16,980 genes were left after filtering. Counts were normalized by weighted trimmed mean of M values (28). To discover the differential genes, edgeR, an R package for differential expression analysis of digital gene expression data (29), was used. Generalized linear model likelihood ratio tests were performed to detect genes that were differentially expressed between groups in each cell type. R

version 4.1.1 (10 August 2021) and the Platform: x86_64-conda-linux-gnu (64-bit) was used. Gene set enrichment analyses (GSEAs) were performed by using the molecular signatures of hallmark gene sets and reactome enrichment gene sets provided by the MSigDB database (http://www.gsea-msigdb.org/). The indicated number of differential expressed genes within the indicated immune cell population derived from WT or RNLS mutant grafts were used as input.

Data and Resource Availability

All data are available from the corresponding author upon reasonable request. Data sets from our scRNAseq experiments are available from the Gene Expression Omnibus (https://www.ncbi.nlm.nih.gov/geo/) under accession number GSE226361.

RESULTS

Rnls Deficiency Modifies β-Cell Metabolism

We previously reported that *Rnls* deletion modifies β-cell vulnerability to stress-induced apoptosis and autoimmunity (7). We had demonstrated the stress-resistant phenotype of *Rnls*-deficient cells both in the mouse NIT-1 β-cell line and in human SC-derived β-cells. To better understand how *Rnls* deletion alters β-cell function and modifies autoimmunity in vivo, we took advantage of the NIT-1 cell line that can be transplanted as a syngeneic graft into NOD mice, a model for autoimmune diabetes. We started by measuring transcriptional changes in NIT-1 cells following *Rnls* deletion. Bulk RNAseq analysis indicated that the loss of *Rnls* impacted the expression of key metabolic targets and pathways (Fig. 1*A* and *B*). Notably, many genes involved in carbohydrate metabolism (e.g., pyruvate kinase M [*Pkm*] and phosphofructokinase [*Pfkl*]) were upregulated, suggesting enhanced glycolysis. Using seahorse measurements as a proxy for metabolic flux, we found that *Rnls* deficiency was associated with a higher basal ECAR, indicative of increased glycolytic activity (Fig. 1*C*). Basal oxygen consumption rate (OCR) was not altered by *Rnls* deletion and highlights a pathway-specific metabolic shift (Fig. 1*D*).

Based on reports that tumor metabolism can impact on the phenotype of tumor-infiltrating lymphocytes (13–16), we speculated that metabolic changes in β-cells may similarly affect local T-cell function. To start exploring this notion, we performed in vitro coculture experiments. The presence of NIT-1 β-cells diminished $CD4^+$ T-cell proliferation in response to mitogenic stimuli (Fig. 1*E* and *F*). Significantly, *Rnls* mutant β-cells had a stronger negative effect on T-cell proliferation at all cell concentrations tested. The effect of *Rnls*-deficient cells was even detectable, albeit to a lesser extent, in the absence of cell-cell contact when T cells and β-cells were separated in a transwell system (Fig. 1*F*). These data led us to hypothesize that *Rnls* deletion in β-cells may influence local immune cell activity in the transplant setting we had used previously to identify *Rnls* as a target for β-cell protection (7). Of note, the NIT-1 cell line was derived from a β-cell adenoma (30), and we cannot exclude that our observations are due, in part, to the tumorigenic nature of this model β-cell line.

Rnls Deficiency in β-Cells Changes the Profile of Graft-Infiltrating Immune Cells

To investigate the effect of β-cell *Rnls* deficiency on immune cell function in vivo, we used a transplantation model in which NIT-1 cells are rejected by autoimmunity (7) (Fig. 2*A*). Isogenic WT and *Rnls* mutant (RNLS) β-cells were transplanted subcutaneously on opposite flanks of the same immunodeficient NOD-*Prkdc*^{scid} (NOD.scid) recipient mice. Four days after engraftment of β-cells, autoreactive splenocytes isolated from spontaneously diabetic NOD mice were injected i.v. to induce β-cell killing. Infiltrating immune cells were then collected and characterized by flow cytometry and scRNAseq at different times posttransplantation.

In preliminary experiments, we evaluated the kinetics of immune cell infiltration into β-cell grafts to determine the best time points for in-depth analyses. We also compared graft-infiltrating cells with the immune cell composition in the spleen and pancreas of NOD.scid recipient mice that are repopulated by donor lymphocytes. We found that days 10 and 17 post–splenocyte injection were most suitable for immune cells for analyses (Supplementary Fig. 1). Cell numbers were limiting before day 10, prior to substantial immune infiltration. At later times (day 23), WT grafts were largely destroyed, precluding recovery of sufficient immune cells (data not shown). These first analyses also showed that immune cells in the spleen, pancreas, and WT β-cell grafts had a similar overall profile (Supplementary Fig. 1*A* and *B*).

We went on to characterize graft-infiltrating immune cells in more detail at days 10 and 17. In early infiltrates, T cells had upregulated the activation marker CD69, but only a few $CD4^+$ T cells and no $CD8^+$ T cells had yet acquired an effector/memory phenotype characterized by CD44 upregulation and downregulation of CD45RB (Supplementary Fig. 1*C* and *D*). Later in the autoimmune process, $CD4^+$ T cells were markedly increased and infiltrating cells included many effector/memory T cells, indicating a more established antigen-specific response within the grafts (Supplementary Fig. 1*C* and *D*). Graft-weight measurements confirmed that *Rnls*-deficient β-cells were protected from immune-mediated killing, as reported previously (7) (Fig. 2*B* and *C*). On average, *Rnls* mutant grafts were twice as large as their matched WT counterpart (Fig. 2*B*). As expected, no difference in graft weight was observed in the absence of autoimmunity (Fig. 2*D*).

Next, we compared the immune cell composition between paired WT and *Rnls*-deficient grafts by scRNAseq in addition to flow cytometry. Both methods revealed concordant differences with an elevated frequency of $CD4^+$ T cells and a decrease in natural killer (NK) cells in *Rnls*-deficient grafts early in the immune attack (Fig. 2*E–H*).

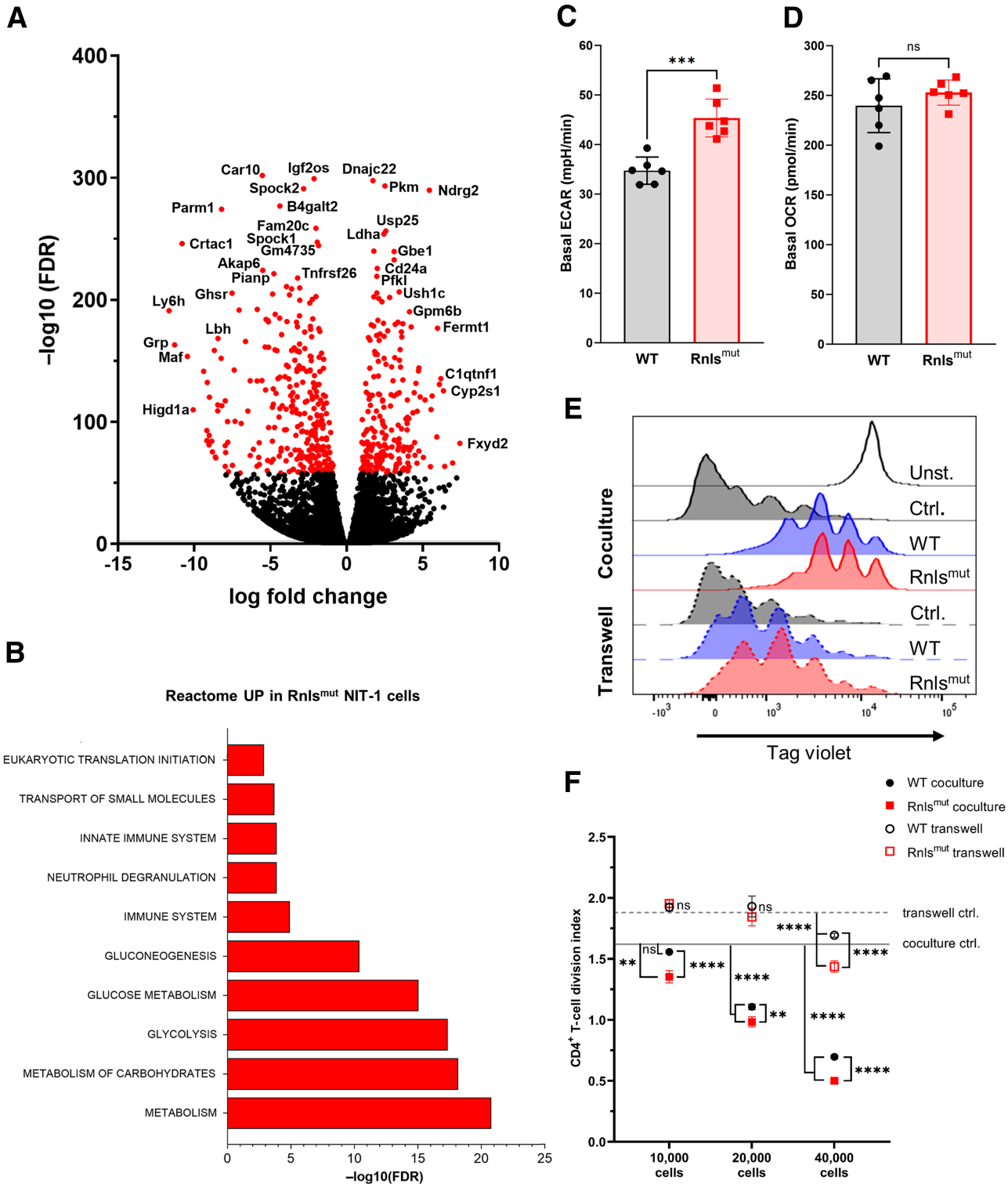

Figure 1—*Rnls* deficiency changes β-cell metabolism. (*A*) Volcano plot showing differential gene expression (DGE) analysis from bulk RNAseq of *Rnls*-deficient NIT-1 β-cells (RNLS) compared with WT control (WT). The 500 most significantly changed genes are indicated in red. Results were obtained using three biological replicates. (*B*) Reactome analysis of the 10 most significantly changed pathways in *Rnls*-deficient β-cells compared with WT cells using the 500 most significant upregulated genes as input. (*C* and *D*) Seahorse metabolic flux assay of WT vs. *Rnls*-deficient NIT-1 cells showing the basal ECAR in *C* and the basal OCR in *D*. Results represent the mean ± SD of one of two independent experiments ($n = 6$). (*E* and *F*) $CD4^+$ T-cell proliferation assay in coculture or transwell culture with indicated cell numbers of WT or *Rnls*-deficient NIT-1 cells. Representative histogram plots in culture with 40,000 NIT-1 cells are shown in *E*. Quantification of the T-cell division index is shown in *F*. The dashed gray line indicates the mean T-cell division index in the absence of NIT-1 cells. Results represent the mean ± SD of one of two independent experiments ($n = 3$). ****$P < 0.0001$, ***$P < 0.001$, **$P < 0.01$, ns $P > 0.05$ (unpaired, two-tailed *t* test).

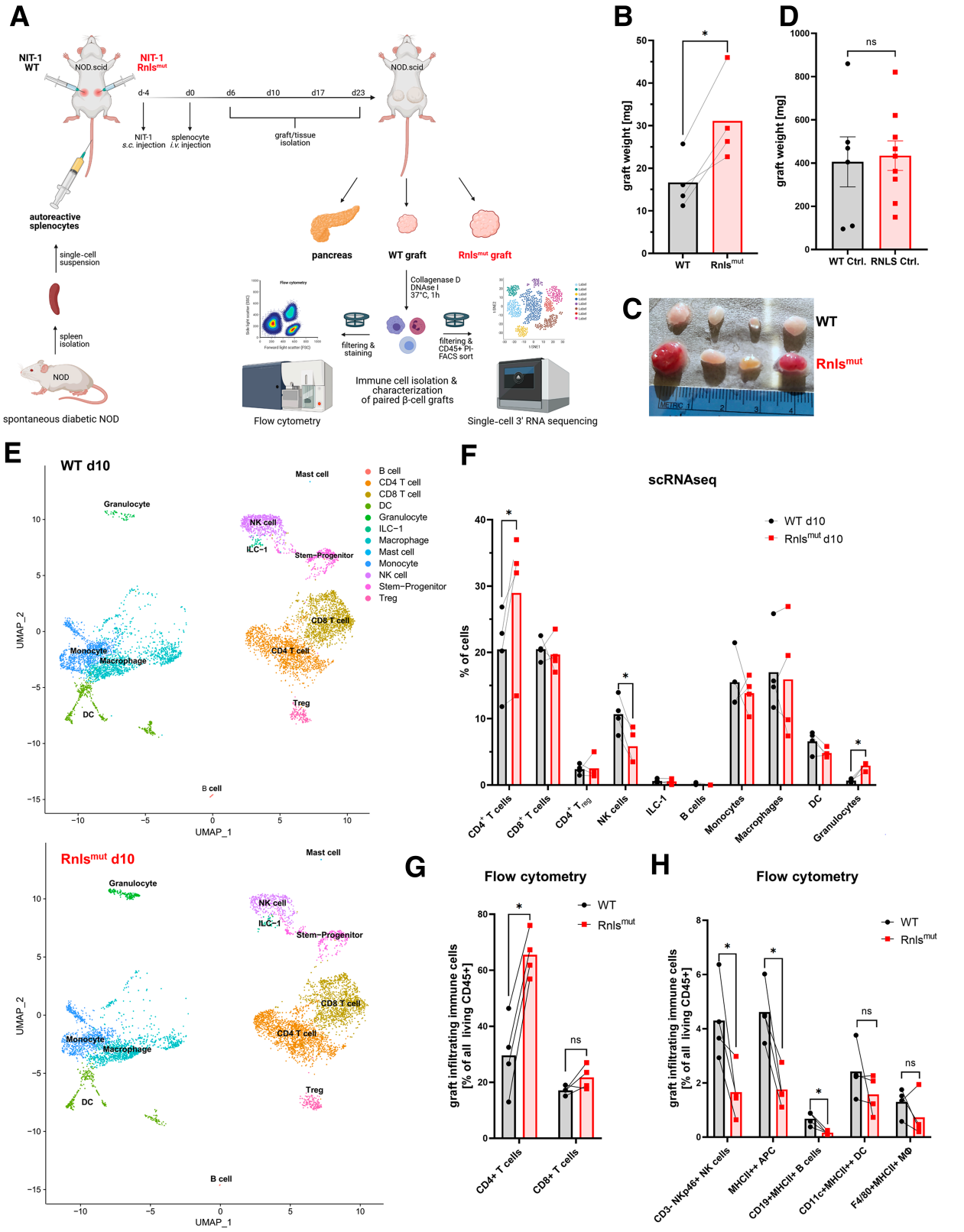

Figure 2—*Rnls* deficiency in β-cell changes the composition of graft-infiltrating immune cells. (*A*) Schematic representation of the experimental design comparing immune cell infiltration of paired WT and *Rnls*-deficient NIT-1 cell grafts; 1.5×10^7 NIT-1 WT or *Rnls* mutant cells were injected subcutaneously (*s.c.*) into opposite flanks of NOD.scid mice, followed by i.v. injection of autoreactive splenocytes 4 days (d) later. The indicated tissues were harvested, and immune cell suspensions were analyzed by scRNAseq or flow cytometry. (*B–D*) Weight (*B* and *D*) and photographs (*C*) of paired grafts from mice with (*B* and *C*) or without (*D*) autoreactive splenocytes injection are shown. Results represent the mean of four paired biological replicates from one of two (*B*) or the mean ± SD of six to seven biological

Very early in the infiltration process, prior to measurable graft weight differences, the frequency of $CD4^+$ T cells was not different between graft genotypes, but NK cells were already enriched in WT grafts (Supplementary Fig. 2*A* and *B*). We also noted a significant increase in granulocytes within protected *Rnls*-deficient grafts, driven by neutrophils and polymorphonuclear myeloid-derived suppressor cells, as asserted by increases in the neutrophil marker Ly6g and the polymorphonuclear myeloid-derived suppressor cells markers Cathepsin D (ctsd), CD84, Arginase 2 (Arg2), and the immune-regulatory gene CD274 that encodes programmed cell death-ligand 1 (PD-L1), all within the granulocyte cluster (data not shown).

Only a very few B cells were detected in the grafts. Notwithstanding their very low number, significantly fewer B cells infiltrated *Rnls*-deficient grafts compared with WT grafts (Fig. 2*H* and Supplementary Fig. 2*C* and *D*). Of note, the profile of immune cells found in WT grafts was very similar to that of immune cells found in the pancreas (Supplementary Fig. 2*D*). In contrast, immune cells in *Rnls*-deficient grafts not only included a higher frequency of $CD4^+$ T cells and fewer NK cells but were also characterized by a marked decrease in MHC class II–expressing cells (Fig. 2*H*). The difference in MHC class II expression was not detectable by scRNAseq (data not shown) but was obvious by flow cytometry, which showed a decrease in the frequency both of MHC class II–expressing APC and of MHC class II cell surface levels (Fig. 2*H* and Supplementary Fig. 2*E* and *F*).

Graft *Rnls* Deficiency Affects the Transcriptional Profile of Infiltrating Immune Cells

After identifying differences in immune cell composition between grafts, we performed differential gene expression analyses on all cells of hematopoietic origin, as defined by CD45 expression (Fig. 3*A*). Genes involved in antigen processing and presentation via MHC class I (e.g., *Tap2*, *H2-D1*) and genes encoding immune-regulatory cytokines such Oncostatin M (*Osm*) and Transforming growth factor beta (*Tgfb1*) were increased within *Rnls* mutant grafts. Hallmark gene expression analysis also indicated that Tgfβ and Tumor necrosis factor alpha (Tnfα) signaling were elevated in *Rnls*-deficient grafts. Notably, we detected a significant increase in glycolytic genes in protected grafts (Fig. 3*B*). Apoptosis and hypoxia signatures were also elevated in immune cells from *Rnls* mutant grafts. These features were again apparent in reactome enrichment analyses that identified cytokine signaling, programmed cell death, regulated necrosis, and apoptosis in $CD45^+$ cells within *Rnls*-deficient grafts (Fig. 3*C*).

Compared with *Rnls*-deficient grafts, immune cells in WT grafts had traits of enhanced RNA regulation exemplified by the upregulation of heterogeneous nuclear ribonucleoprotein M (Hnrnpm), Cms1 ribosomal small subunit homolog (Cmss1), nucleolar RNA helicase 2 (Ddx21), and polyadenylate-binding protein 4 (Pabpc4) (Fig. 3*A*). Several genes related to initiation of protein synthesis such as eukaryotic translation initiation factor 2 subunit beta (Eif2s2) and eukaryotic translation initiation factor 3, subunit J1 (Eif3j1), were also upregulated in WT graft-infiltrating immune cells (Fig. 3*A*). Reactome enrichment analysis confirmed the intensification of RNA metabolism including rRNA processing, processing of capped intron containing pre-mRNA, and mRNA splicing, as well as reinforced protein translation initiation (Fig. 3*C*). Furthermore, hallmark gene expression analysis in WT graft-immune cells suggested that immunometabolism was enriched for oxidative phosphorylation markers and that mammalian target of rapamycin complex 1 (mTORC1) pathway components were upregulated (Fig. 3*B*). This was aligned with the reactome analysis showing enhanced respiratory electron transport, complex I biogenesis, and ATP synthesis in WT graft immune cells (Fig. 3*C*). Of interest, increased *Tgfb1* expression within *Rnls* mutant grafts originated from $CD4^+$ T cells and myeloid cells (Fig. 3*D*), and this was confirmed by flow cytometry showing that latency-associated peptide (LAP)/TGFβ1 was upregulated on the surface of these cells (Fig. 3*F–I*).

In addition to the early time point at day 10, we also investigated immune cell infiltration and global gene expression profiles at day 17. At this later stage, grafts were markedly smaller, but *Rnls* mutant grafts remained approximately twofold larger than WT grafts (Fig. 4*A*). Of note, the differential immune cell infiltration shown in Fig. 2 for day 10 was no longer detectable at day 17, except for a minor increase in macrophages and a small decrease in NK cells within *Rnls*-deficient grafts (Fig. 4*B*). Overall, the $CD8^+$ T-cell fraction was decreased from 20% down to 10%, while the macrophage population became dominant (20% of all $CD45^+$ cells at day 10 increased to 50% at day 17) (compare Figs. 2*F* and 4*B*). Consistent with these changes, global differential gene expression analysis showed that several macrophage-related genes, including Apolipoprotein E (Apoe) and CC-chemokine ligand 8 (Ccl8), were increased at day 17 (Fig. 4*C*). Critically, reactome enrichment analysis indicated that immune cells in *Rnls* mutant grafts had features of cellular starvation and

replicates from two combined experiments (*D*). (*E*) UMAP showing the distribution of immune cell subpopulations within all *Rnls*-deficient (top) or WT (bottom) grafts. (*F*) Quantification of immune cell subpopulations derived from four paired grafts as determined by scRNAseq. Results represent the mean of four paired biological replicates. (*G*) Quantification of indicated immune cells derived from paired WT and *Rnls*-deficient grafts as determined by flow cytometry. Results represent the mean of four paired biological replicates. $*P < 0.05$, ns $P > 0.05$ (paired two-tailed *t* test). Data obtained from scRNAseq (*E* and *F*) and from flow cytometry (*G* and *H*) are from independent experiments.

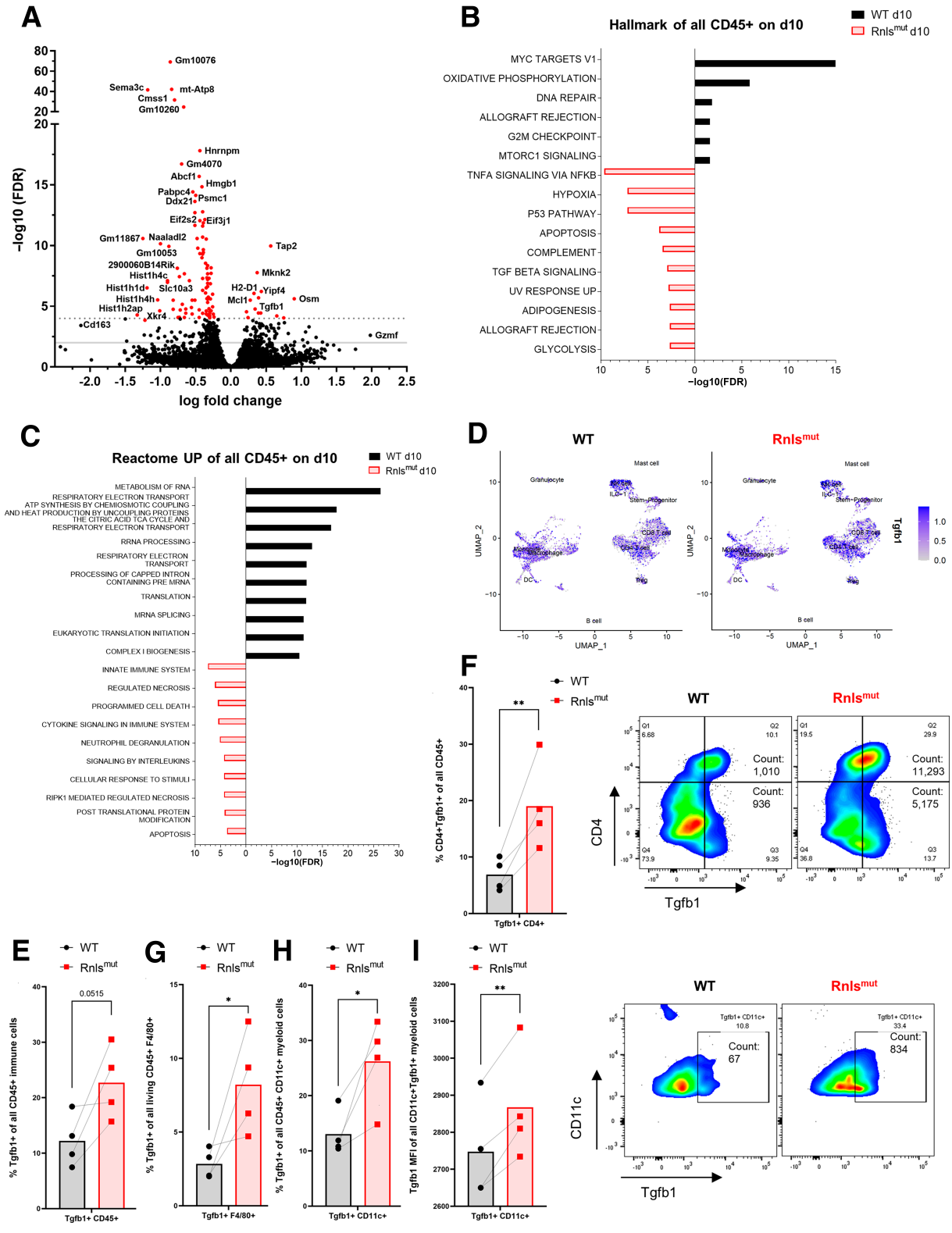

Figure 3—*Rnls*-deficient β-cells cause global transcriptional changes in graft-infiltrating immune cells. (*A*) Volcano plot showing differential gene expression (DGE) between CD45$^+$ cells sorted from *Rnls*-deficient and WT grafts 10 days after splenocyte transfer. The most significantly changed genes are indicated in red (–log10 [FDR] ≥ 4, cutoff shown by dotted gray line). The solid gray line: –log10 (FDR) ≥ 2. (*B*) Hallmark gene expression analysis and (*C*) reactome analysis showing the 10 most significantly changed pathways (–log10 [FDR] ≥ 2). (*D*) UMAP of *Tgfb1* expression in CD45$^+$ cells from *Rnls* mutant (left) and WT (right) grafts. (*E–H*) Quantification and representative contour plots of the frequency of LAP/Tgfb1 surface expression in CD45$^+$ cells (*E*), CD4$^+$ T cells (*F*), CD45$^+$F4/80$^+$ (*G*) and CD45$^+$CD11c$^+$ myeloid cells (*H* and *I*) analyzed by flow cytometry. Results represent the mean of four paired biological replicates. *$P < 0.05$, **$P < 0.01$ (paired, ratio two-tailed *t* test). Data from scRNAseq and flow cytometry are derived from independent experiments.

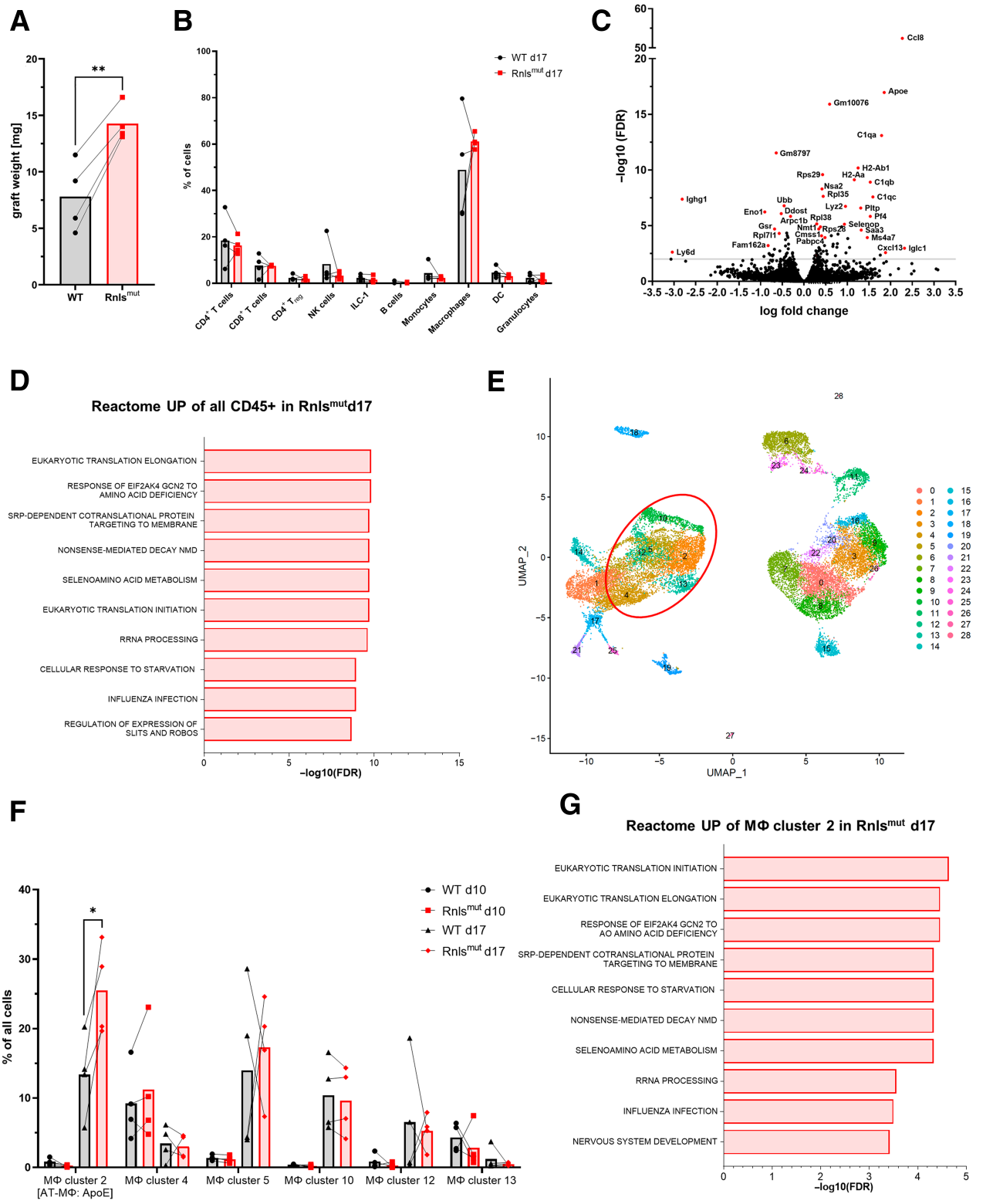

Figure 4—Immune cells adopt features of cellular response to starvation in *Rnls*-deficient grafts and are enriched for an adipose-tissue-like macrophage (Mϕ) population. (*A*) Quantification of graft weight from paired WT and RNLS-deficient grafts isolated at day 17. Results represent the mean of four paired biological replicates. $^{**}P < 0.01$ (paired, two-tailed *t* test). (*B*) Frequency of immune cell subpopulations identified by scRNAseq. (*C*) Volcano plot showing DGE in $CD45^+$ cells. Red circles denote genes with –log10 (FDR) ≥ 2 (solid gray line). (*D*) Reactome analysis of $CD45^+$ cells at day 17. The 10 most significantly upregulated pathways (–log10 [FDR] ≥ 2) are shown. (*E*) UMAP analysis showing 28 unique clusters. (*F*) Quantification of all Mϕ clusters identified at both day 10 (early infiltrated) and day 17 (late infiltrated). Results represent the mean of four paired biological replicates. $^{*}P < 0.05$ (paired, multiple two-tailed *t* test). (*G*) Reactome analysis of Mϕ cluster 2 at day 17. The 10 most significantly upregulated pathways (–log10 [FDR] ≥ 2) are shown.

amino acid deficiency (Fig. 4*D*). Cluster analysis for all combined samples (including day 10 and day 17 from both genotypes) identified 28 unique immune cell clusters (Fig. 4*E*). The same traits of cellular response to starvation and response of EIF2K4 to amino acid starvation was observed in almost all individual cell populations (data not shown), suggesting a global metabolic effect on graft-infiltrating immune cells.

The large macrophage (Mϕ) population was composed of six distinct clusters (Mϕ clusters 2, 4, 5, 10, 12, and 13). Mϕ clusters 4 and 13 were dominant at day 10. At day 17, clusters 2 and 5 became most prominent (Fig. 4*F*). Mϕ cluster analysis also revealed a twofold enrichment of Mϕ cluster 2 in *Rnls*-deficient grafts, and this population was characterized by high expression of ApoE with traits of an adipose tissue Mϕ (AT-Mϕ) identity (Fig. 4*F* and Supplementary Fig. 3*A*–*C*). Reactome enrichment analysis of AT-Mϕ cluster 2 suggested that these cells were less inflammatory than Mϕ cluster 4 (Supplementary Fig. 3*D*). In *Rnls* mutant grafts, AT-Mϕ cluster 2 cells again displayed a profile corresponding to a starvation and amino acid deficiency phenotype compared with WT grafts (Fig. 4*G*).

Rnls Deficiency Causes an Accumulation of $CD4^+$ T Cells Coexpressing *Tgfb1* and *Ifng*

Flow cytometry and scRNAseq analyses had shown an enrichment of $CD4^+$ T cells within *Rnls* mutant β-cell grafts early in the autoimmune process (see Fig. 2*E*–*G*). $CD4^+$ T cells could be divided into four distinct clusters (clusters 0, 7, 8, and 22) (Fig. 4*E*). Cluster 0 was dominant early in graft infiltration, while cluster 8 cells became the most frequent $CD4^+$ T cells at the later time point (Fig. 5*A*). Reactome analysis demonstrated distinct metabolic and inflammatory features in clusters 0 and 8 (Fig. 5*B*). Because cluster 0 was significantly increased early in *Rnls*-deficient β-cell grafts (Fig. 5*A*), we analyzed the differential gene expression profile of this cluster in more detail. Whereas $CD4^+$ T cells in cluster 0 had upregulated genes involved in the interferon γ (*Ifng*) response in WT grafts, the same cell cluster had a regulatory phenotype in *Rnls*-deficient grafts, with a signature for TGFβ signaling (Fig. 5*C*). The metabolic markers of cluster 0 cells changed from oxidative phosphorylation, activated citric acid cycle, and respiratory electron transfer pathways in WT grafts toward enhanced lipid metabolism in *Rnls* mutant grafts (Fig. 5*C* and *D*). Of note, Uniform Manifold Approximation and Projection (UMAP) analysis for key cytokines and surface molecules showed that cluster 0 cells coexpressed Interferon gamma (*Ifng*), *Tgfb1*, and, to a lesser degree, Cytotoxic T-lymphocyte-associated protein 4 (*Ctla4*) and Interleukin 2 receptor alpha (*Il2ra*) (Fig. 5*E*–*I*). GSEA suggested that the gene expression profile of cluster 0 was most similar to a $Foxp3^+$ regulatory T-cell (T_{reg}) population (Treg_4_FP3+_Nrplo_Co) described in the ImmGen ULI RNA-Seq database (Supplementary Fig. 4), even though cluster 0 cells did not express *Foxp3* (data not shown).

Rnls-Deficient Graft Protection Is Associated With Increased PD-1 Expression on T Cells, but PD-L1 Overexpression in β-Cells Is Only Marginally Protective Against Autoimmunity

In addition to the gene expression profile analyses performed by scRNAseq, T-cell phenotypes were investigated by staining for key cell surface markers in β-cell grafts and their corresponding draining lymph nodes at day 17 (Fig. 6*A*–*D*). Fewer $CD4^+$ T cells within *Rnls* mutant grafts expressed the short-term activation marker CD69, while more cells had adopted an effector memory phenotype ($CD44^+CD45RB^{lo}$) (Fig. 6*A*). This enrichment of effector memory $CD4^+$ T cells was observed within the *Rnls* mutant grafts and not in the corresponding draining lymph nodes, suggesting a localized change (Fig. 6*B*). The overall frequency of effector memory $CD4^+$ T cells was high (70–90% of all $CD4^+$ cells), whereas only 20–40% of all $CD8^+$ T cells had an effector memory phenotype (Fig. 6*A* and *B*). Notably, we measured a twofold increase in the frequency of PD-1^+CD8^+ T cells in *Rnls*-deficient versus WT grafts, amounting to approximately 40% of all $CD8^+$ T cells in protected grafts (Fig. 6*A* and *C*). This effect was not exclusive to the graft environment, because T cells in *Rnls* graft draining lymph nodes had also upregulated PD-1 surface expression (Fig. 6*B*). PD-1 surface expression declined over time in WT grafts, but not in *Rnls* mutant grafts (Fig. 6*D*). This observation led us to speculate that the higher frequency of PD-1–expressing T cells may be important for graft survival and that this feature could be exploited to further protect grafts against autoimmune killing. To test this idea, we generated WT and *Rnls* mutant NIT-1 cells that overexpress PD-L1 (Fig. 6*E*). We reasoned that increasing the availability of PD-L1 within the graft could be protective, as claimed previously (5). Of note, NIT-1 did not express measurable amounts of PD-L1 prior to transduction with lentiviral PD-L1 constructs. We proceeded to compare the survival of PD-$L1^-$ and PD-$L1^{hi}$ β-cells independently for both WT and *Rnls* mutant cells in cotransplant experiments where grafts were again challenged with immune cells from diabetic NOD mice (see Fig. 6*F* for schematic of experimental design). Note that graft size was analyzed at day 20, to allow for effective immune-mediated killing in the absence of genetic protection. Unexpectedly, the overexpression of PD-L1 only had a very modest effect on the survival of WT grafts, and did not provide any protection to *Rnls* mutant β-cell grafts. (Fig. 6*G*). To ascertain that WT NIT-1 did not up-regulate PD-L1 in vivo after transplantation, which could confound our interpretation of these data, we performed another transplantation to measure PD-L1 ex vivo (Fig. 6*H*–*J*). For ease of NIT-1 cell identification in explanted grafts, we prelabeled cells with CFSE. We detected no significant PD-L1 expression on the surface of transplanted NIT-1 cells, and PD-L1 expression was restricted to $CD45^+$ cells within explanted grafts. Collectively, these data suggest that PD-L1 expression in NIT-1

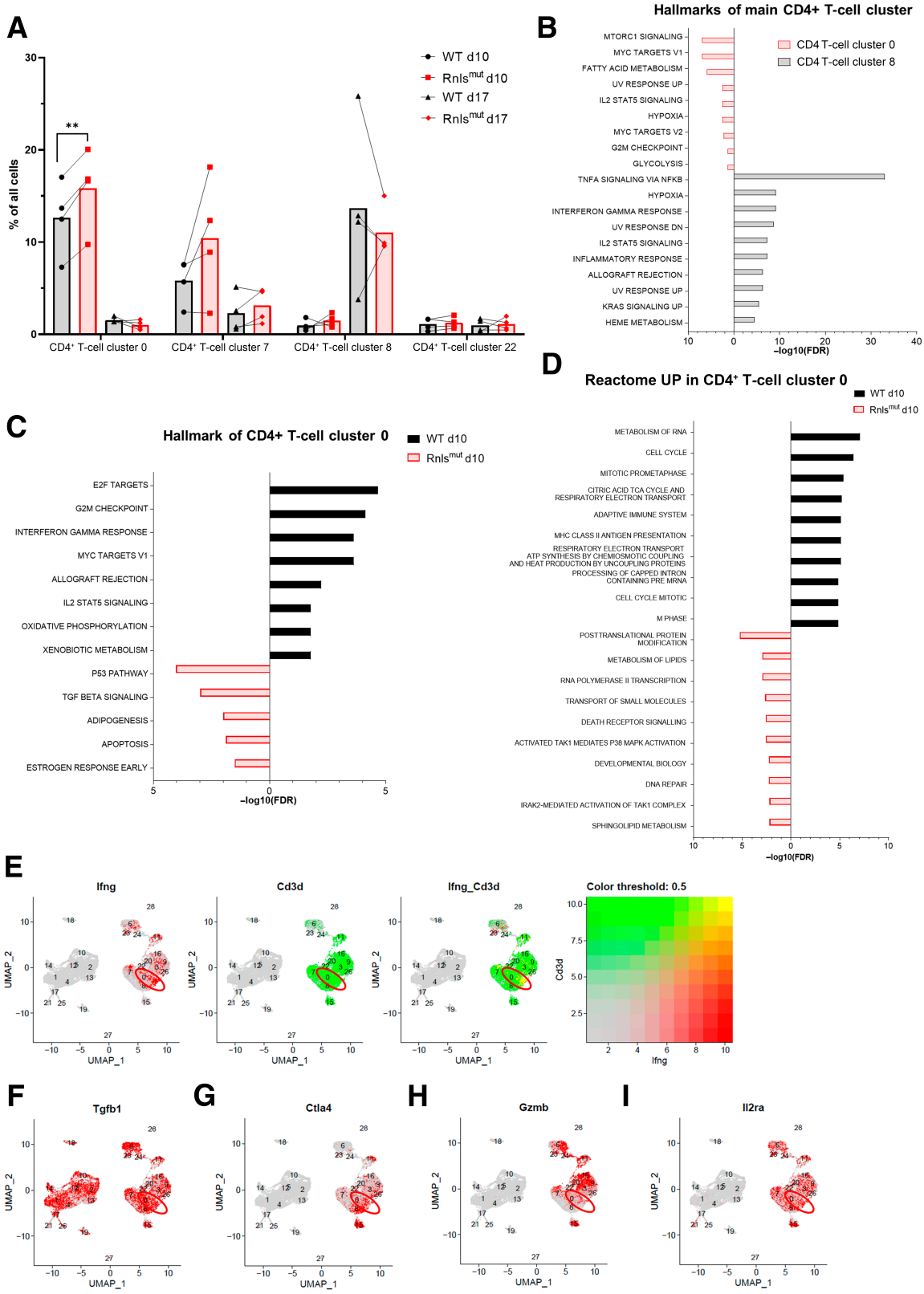

Figure 5—*Rnls*-deficient grafts accumulate CD4$^+$ T cells that coexpress *Tgfb1* and *Ifng*. (*A*) Frequency of all CD4$^+$ T-cell clusters in WT and *Rnls*-deficient grafts at days 10 and 17. Results represent the mean of four paired biological replicates. $^{**}P < 0.01$ (paired, two-tailed *t* test). (*B*) Reactome analysis of the two main CD4$^+$ T-cell clusters, 0 and 8. (*C* and *D*) Hallmark gene expression analysis (*C*) and reactome analysis (*D*) of cluster 0. The 10 most significantly changed pathways (–log10 [FDR] ≥ 2) are shown. (*E–I*) UMAP analyses showing the expression of indicated genes in all 28 clusters. (*E*) Expression and coexpression of *Ifn*γ and *Cd3*δ across clusters. (*F–I*) Expression of *Tgfb*, *Ctla4*, *Gzmb*, and *Il2ra*, respectively, across clusters.

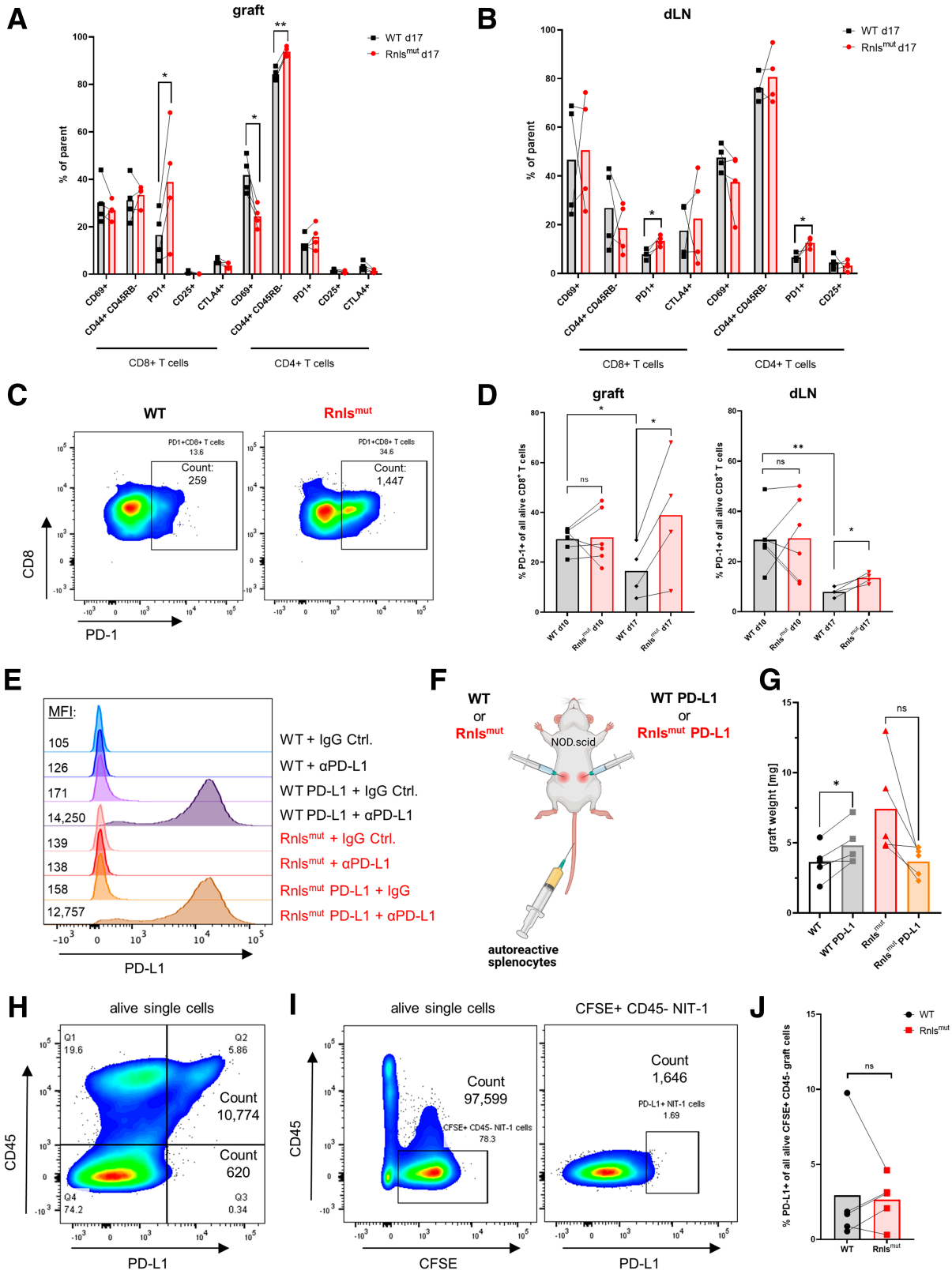

Figure 6—Graft protection is associated with PD-1 expression on CD8$^+$ T cells, but PD-L1 overexpression on β-cells does not improve graft survival. (*A* and *B*) Quantification of surface marker expression on CD8+ T cells (left) and CD4+ T cells (right) in WT (black) and *Rnls*-deficient (red) grafts (*A*) and in corresponding draining lymph nodes (dLN) (*B*) on day 17. (*C* and *D*) Representative flow cytometry results (*C*) and summary data (*D*) for PD-1 expression on the surface of CD8$^+$ T cells on day 10 (WT: black squares; *Rnls* deficient: red circles) and day 17 (WT: black diamonds; *Rnls* deficient: red triangles) in grafts (*D*, left) and dLN (*D*, right). In *A*–*D*, results show the mean of four paired biological replicates. *$P < 0.05$, **$P < 0.01$, ns $P > 0.05$. (*E*) Representative flow cytometry data for anti–PD-L1 staining of NIT-1

β-cells only plays a minor—if any—role in preventing immune-mediated killing.

Rnls Mutant β-Cell Grafts Harbor a High Frequency of MHC Class II^{low} PD-L1^{+} APC, and PD-L1 Blockade Effectively Eradicates Transplanted β-Cells

The most prominent changes in the immune cell composition within protected *Rnls* mutant grafts included a decrease in MHC II^{+} cells. scRNAseq cluster analyses further showed that two dendritic cell (DC) clusters in particular were decreased in their frequency. These were DC cluster 17, with a gene expression profile corresponding to conventional DC subset 2 (cDC2), and cluster 25, corresponding to plasmacytoid DC (pDC) (Fig. 7*A* and *B* and Supplementary Fig. 5). Antigen-presenting cells in *Rnls*-deficient grafts had lower MHC class II and higher PD-L1 expression (Fig. 7*C*–*E*). Because we had found that overexpression of PD-L1 on β-cells themselves had little effect on graft survival, we posited that PD-L1 expression in cells of hematopoietic origin may be more critical in the control of autoimmunity. To test this, we administered PD-L1 blocking antibody to β-cell graft recipients after injection of diabetogenic immune cells. Systemic PD-L1 inhibition dramatically accelerated the elimination of both WT and *Rnls* mutant grafts (Fig. 7*F* and *G*). In the setting of PD-L1 blockade, *Rnls*-deficient β-cells no longer had a survival advantage compared with WT cells. Our results highlight the fundamental importance of the PD-1/PD-L1 pathway in suppressing immune-mediated killing but also show that PD-L1 expression in β-cells plays a negligible role in protecting grafted β-cells against autoimmunity.

DISCUSSION

In this study, we investigated the interaction between *Rnls*-deficient β-cells and immune cells in a model for β-cell transplantation in autoimmune diabetes. The exact mechanism by which *Rnls* deletion protects β-cells against autoimmunity is still unclear. However, our observation that the loss of *Rnls* impacted cellular metabolism led us to hypothesize that mutant β-cells may modify their microenvironment to suppress immune function. It is now well established that metabolic interactions between cancer cells and immune cells contribute to tumor immune evasion (13–16). We posited that metabolic changes in β-cells could generate a similarly protective microenvironment. In support of this hypothesis, we found that β-cells cocultured with T cells were not inert and diminished the proliferative response of stimulated T cells. This effect was accentuated when *Rnls*-deficient β-cells were used, and inhibition of T-cell proliferation was still apparent in a transwell setting, where only soluble mediators could be at play. These preliminary results prompted us to examine β-cell–immune cell interactions in the pathophysiological setting of autoimmune diabetes using a transplant approach. We found that *Rnls*-deficient β-cells modified local immune function. Our experimental system comparing paired WT and mutant grafts within the same animal allowed us to conclude that the protective effects of *Rnls* deletion are not systemic and do not extend to distant sites. Instead, key changes in the composition of graft-infiltrating immune cells and in their transcriptional profile were confined to mutant grafts, and, to a lesser extent, to the nearby draining lymph nodes.

The composition of infiltrating immune cells was similar in WT and *Rnls*-deficient grafts, albeit with a few notable differences. First, it is worth pointing out that we did not find a gross numerical difference in graft-infiltrating immune cells overall. *Rnls* deficiency does not simply prevent graft infiltration. Instead, we measured a relative increase in the proportion CD4^{+} T cells and a significant decrease in both the frequency and quality of MHC II–expressing antigen-presenting cells. We propose that a change in the quality of the immune response, and not its amplitude, underlies graft survival. It is noteworthy that macrophages become the dominant cell type as graft autoimmunity progresses, and our data are reminiscent of scRNAseq analyses by Unanue and colleagues (31), who described a large population of macrophages within the pancreatic islets of NOD mice. In this regard, we suggest that our β-cell graft model replicates key aspects of the original immune attack that causes diabetes in the mouse model. This is further underscored by our finding that the compositions of immune populations in the pancreas and WT grafts were very similar in our experiments. An interesting difference is the near-complete absence of B cells in our β-cell transplantation model, in stark contrast to data from infiltrated islets that harbor sizeable B-cell populations at all stages of disease (31). Second, it is clear from our transcriptional analyses that the overall function and the metabolic markers of infiltrating immune cells are impacted by β-cell *Rnls* deficiency. Most notably, we found signatures of cellular starvation and of a response to amino acid deficiency in all cells of hematopoietic origin in *Rnls* mutant grafts at an advanced stage of infiltration (day 17). Already at the earlier time point (day 10), immune cell metabolic markers diverged between WT and *Rnls*-deficient grafts, with a shift from a signature of oxidative phosphorylation to a more glycolytic transcriptional profile, respectively. Of importance, our interpretation that

cells transduced or not with lentivirus encoding PD-L1. Isotype control staining (IgG) is shown for comparison. MFI, median fluorescence intensity. (*F* and *G*) Schematic representation of the experimental design (*F*) and graft weight for indicated conditions 20 days after adoptive transfer of autoreactive splenocytes (*G*). (*H*–*J*) Ex vivo analysis of CFSE-labeled NIT-1 cells 10 days after splenocyte transfer. Representative flow cytometry data of PD-L1 expression on explanted graft cells (*H*) and representative gating strategy (*I*) are shown, together with quantification of PD-L1 expression on CFSE^{+}CD45^{-} NIT-1 cells of the indicated genotype (*J*). Results represent the mean of five paired biological replicates from one of two independent experiments. *$P < 0.05$, ns $P > 0.05$ (multiple paired, two-tailed *t* test).

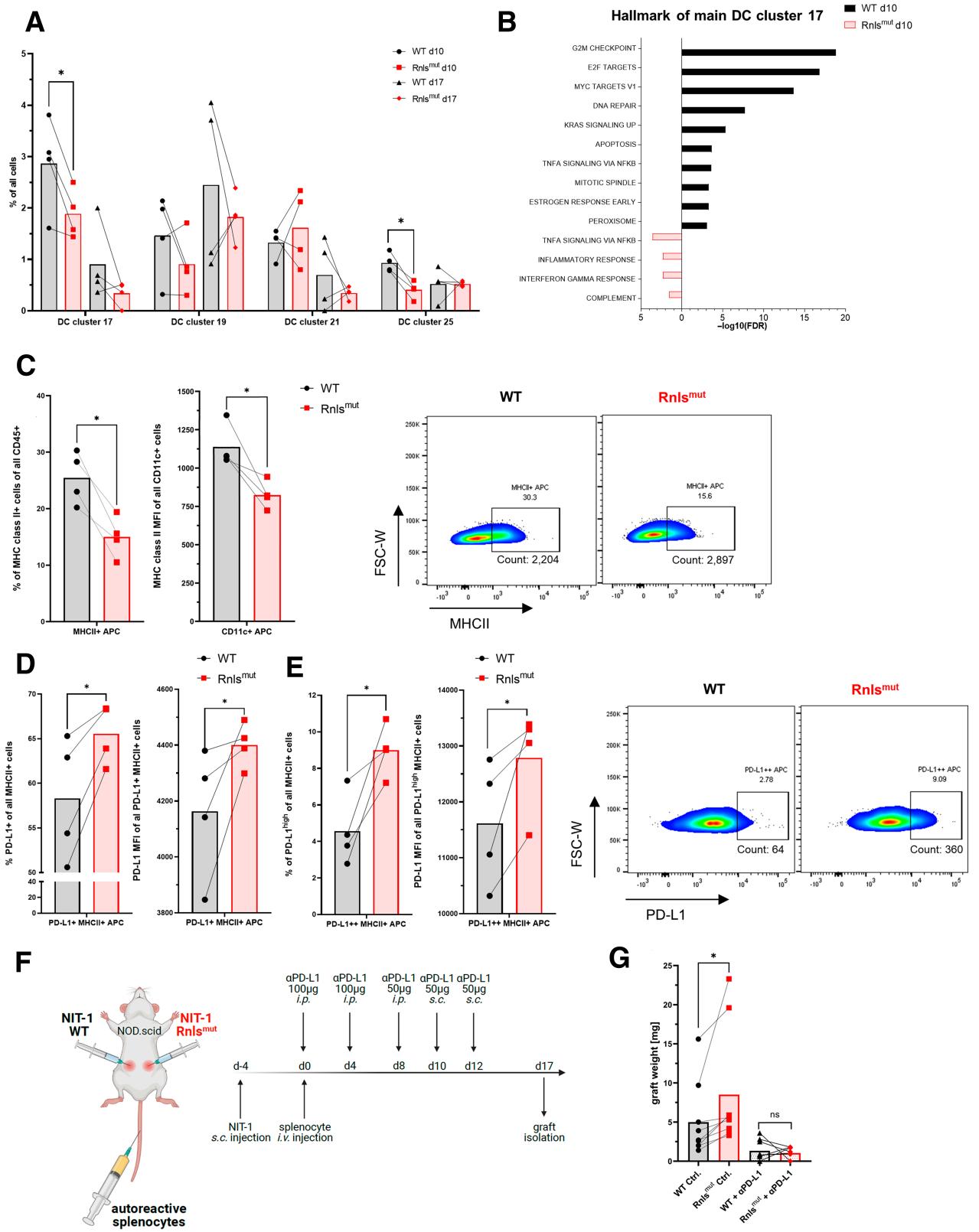

Figure 7—*Rnls*-deficient grafts harbor fewer MHC class II$^+$ and more PD-L1$^+$ immune cells. (*A*) Frequency of all DC cluster identified in paired WT and *Rnls*-deficient grafts. (*B*) Hallmark gene expression analysis of DC cluster 17. (*C*) Summary data (left) and representative flow cytometry (right) for MHC class II expression on infiltrating CD45$^+$ cells. (*D*) Frequency (left) and median fluorescence intensity (MFI) (right) for PD-L1 expression on MHC II$^+$ cells. (*E*) Frequency (left), PD-L1 MFI (middle), and representative flow cytometry (right) for PD-L1^{high} MHC II$^+$ cells. (*F* and *G*) Experimental design (*F*) used to test the effect of PD-L1 blockade on graft survival (*G*); *s.c.*, subcutaneous. Results represent the mean of 4 (*A* and *C*–*E*) or 11 (*G*) paired biological replicates. *$P < 0.05$ (paired [*A* and *G*] or paired ratio [*C*–*E*], two-tailed *t* test).

the metabolic state of immune cells is altered has limitations because metabolic activity largely depends on enzymatic activity and pathway flux and not merely on gene expression. Furthermore, oxidative phosphorylation has repeatedly been associated with anti-inflammatory cellular states, particularly in macrophages. On the other hand, a recent study of tissue macrophages also demonstrated that impairing oxidative phosphorylation depleted proinflammatory tissue-associated macrophages (32). It remains to be demonstrated whether glycolysis or oxphos are strictly associated with proinflammatory or anti-inflammatory immune phenotypes. The data we present herein are descriptive, and further study is needed to address this question mechanistically.

In parallel, we found evidence for diminished inflammatory signatures within protected *Rnls* mutant grafts where TGFβ expression and signaling was significantly increased, for example. These observations suggest that the resistance to immune-mediated killing of *Rnls*-deficient β-cells does not derive from a single discrete pathway but may rather stem from a global shift in the inflammatory status of infiltrating immune cells. This is supported by the many changes we observed in different cell populations, including $CD4^+$ T cells, $CD8^+$ T cell, macrophages, and DCs. In addition, the frequency of minor populations (e.g., NK cells, granulocytes) whose role in β-cell killing is still poorly defined was also impacted by *Rnls* deletion in β-cells.

Notwithstanding the seemingly broad effect of *Rnls* mutation on immune metabolism and function within the graft, we also tested a specific immune modulatory pathway that had been implicated in type 1 diabetes previously (33–36). We had measured a significant increase in the frequency of PD-1^+ cells within the $CD8^+$ T-cell compartment in *Rnls*-deficient grafts. This well-characterized inhibitory molecule is known to contribute to immune regulation in tissue immunity, particularly in the context of tumor immunity but also in autoimmune diabetes (33,34,37). Others had claimed that PD-L1 overexpression in β-cells was highly protective against immune-mediated killing (5). We speculated that this protective effect would be particularly strong in the context of elevated PD-1 expression on T cells. However, we found that overexpressing PD-L1 in β-cells in our experimental model provided very little, if any, survival advantage. Yet, our observation that complete PD-L1 blockade led to rapid destruction of both WT and *Rnls*-deficient grafts suggested that the PD-1/PD-L1 pathway is indeed a key regulator of β-cell autoimmunity. We would argue that it is the expression of PD-L1 in antigen-presenting cells, and not on the surface of the β-cells themselves, that determines the intensity of the attack on β-cells. This would be consistent with our observation that PD-L1 expression was significantly increased in antigen-presenting cell populations in protected grafts.

Overall, our study demonstrates that protection of transplanted β-cells does not require the exclusion of immune cells from the graft. Instead, the immune response to grafted β-cells can be modulated broadly, and we propose that perturbations of β-cell metabolism can endow the graft microenvironment with immune-suppressive features. Of note, we used NIT-1 cells as a model β-cell line because they are syngenic with the best rodent model for T1D. However, it must be pointed out that the NIT-1 cell line was derived from a β-cell adenoma in NOD mice that expressed the SV40 large T-antigen under the control of the rat insulin promoter (30). As such, NIT-1 cells may possess some tumor-like characteristics, and this could partially confound our interpretation that (physiological) β-cell metabolism impacts immune function within the pancreatic islet or within a β-cell graft. Notwithstanding, in earlier work, we had shown that deletion of *Rnls* in primary mouse islets provided some degree of protection against autoimmunity (7), suggesting that our observations overall do not derive from the tumorigenic nature of NIT-1 cells.

Determining what factors mediate the immune modulation we measured in *Rnls*-deficient grafts will necessitate a systematic approach and will undoubtedly prove challenging. Nevertheless, our findings are encouraging because they show that β-cell autoimmunity can be substantially slowed without directly modifying antigen presentation or immune-stimulatory or immune-inhibitory pathways (CTLA-4, PD-1, SIRPα, etc.). This strategy could help preserve immune surveillance of transplanted β-cells engineered to withstand autoimmunity. Entirely preventing immune recognition poses the risk of creating a reservoir for infection or a source for immune-evasive tumors. We speculate that the protection afforded by *Rnls* deletion depends on metabolic changes that would likely be perturbed during infection or the emergence of oncogenicity within protected cells, thereby restoring the ability of the immune system to rid the body of infected or cancerous cells.

In conclusion, we have shown that the protection against autoimmunity afforded by *Rnls* deletion in β-cells is associated with metabolic changes both within β-cells themselves and in immune cells recruited to the site of transplantation. The broad immune modulation effected by *Rnls* deficiency indicates that β-cell protection may be achievable by manipulation of the graft microenvironment. A detailed search for factors derived from *Rnls*-deficient β-cells that modify immune metabolism and function could yield novel factors to manipulate immunity.

Acknowledgments. In particular, the authors would like to acknowledge the expert help of Drs. Jonathan Dreyfuss and Hui Pan (Joslin Diabetes Center Bioinformatics Core) with scRNAseq analyses. The authors also thank Jenna Collier for advice on T-cell scRNAseq methods.

Funding. The authors thank the Joslin Flow Cytometry core (funded in part by National Institutes of Health National Institute of Diabetes and Digestive and Kidney Diseases grant P30DK036836) and the Joslin Bioinformatics core for support of this project. K.B. and T.M. were supported, in part, by postdoctoral fellowships from the Mary K. Iacocca Foundation. This project was also supported by National Institutes of Health National Institute of Diabetes and Digestive and Kidney Diseases grant R01DK120445 awarded to P.Y. and S.K.

Duality of Interest. P.Y. and S.K. are inventors on a patent application filed by the Joslin Diabetes Center that relates to the targeting of *RNLS* for the protection of transplanted SC islets. No other potential conflicts of interest relevant to this article were reported.

Author Contributions. K.B. performed transplantation, flow cytometry, and scRNAsep experiments; analyzed data; and wrote the manuscript. T.M. performed metabolic assays. T.S. generated mutant cells lines. B.M. performed transplant experiments and assisted with animal work. E.P.C. performed RNAseq and analyzed data. N.M. and Y.-C.L. generated reagents. P.Y. provided supervision for some of the work, and analyzed the data. S.K. supervised the project, analyzed data, and wrote the manuscript. All authors reviewed the final manuscript and approved submission. S.K. is the guarantor of this work and, as such, had full access to all the data in the study and takes responsibility for the integrity of the data and the accuracy of the data analysis.

References

1. Brusko TM, Russ HA, Stabler CL. Strategies for durable β cell replacement in type 1 diabetes. Science 2021;373:516–522
2. Melton D. The promise of stem cell-derived islet replacement therapy. Diabetologia 2021;64:1030–1036
3. Deuse T, Hu X, Gravina A, et al. Hypoimmunogenic derivatives of induced pluripotent stem cells evade immune rejection in fully immunocompetent allogeneic recipients. Nat Biotechnol 2019;37:252–258
4. Han X, Wang M, Duan S, et al. Generation of hypoimmunogenic human pluripotent stem cells. Proc Natl Acad Sci USA 2019;116:10441–10446
5. Yoshihara E, O'Connor C, Gasser E, et al. Immune-evasive human islet-like organoids ameliorate diabetes. Nature 2020;586:606–611
6. Deuse T, Tediashvili G, Hu X, et al. Hypoimmune induced pluripotent stem cell-derived cell therapeutics treat cardiovascular and pulmonary diseases in immunocompetent allogeneic mice. Proc Natl Acad Sci USA 2021;118:e2022091118
7. Cai EP, Ishikawa Y, Zhang W, et al. Genome-scale in vivo CRISPR screen identifies RNLS as a target for β-cell protection in type 1 diabetes. Nat Metab 2020;2:934–945
8. Beaupre BA, Hoag MR, Roman J, Försterling FH, Moran GR. Metabolic function for human renalase: oxidation of isomeric forms of β-NAD(P)H that are inhibitory to primary metabolism. Biochemistry 2015;54:795–806
9. Moran GR. The catalytic function of renalase: a decade of phantoms. Biochim Biophys Acta 2016;1864:177–186
10. Kierans SJ, Taylor CT. Regulation of glycolysis by the hypoxia-inducible factor (HIF): implications for cellular physiology. J Physiol 2021;599:23–37
11. Wang X, Eno CO, Altman BJ, et al. ER stress modulates cellular metabolism. Biochem J 2011;435:285–296
12. Balsa E, Soustek MS, Thomas A, et al. ER and nutrient stress promote assembly of respiratory chain supercomplexes through the PERK-eIF2α axis. Mol Cell 2019;74:877–890.e6
13. Lau AN, Vander Heiden MG. Metabolism in the tumor microenvironment. Annu Rev Cancer Biol 2020;4:17–40
14. Lim AR, Rathmell WK, Rathmell JC. The tumor microenvironment as a metabolic barrier to effector T cells and immunotherapy. eLife 2020;9:e55185
15. Watson MJ, Vignali PDA, Mullett SJ, et al. Metabolic support of tumour-infiltrating regulatory T cells by lactic acid. Nature 2021;591:645–651
16. Notarangelo G, Spinelli JB, Perez EM, et al. Oncometabolite d-2HG alters T cell metabolism to impair $CD8^+$ T cell function. Science 2022;377:1519–1529
17. Zheng, G. X. Y. et al. Massively parallel digital transcriptional profiling of single cells. Nat Commun 2017;8:14049
18. Lun ATL, Riesenfeld S, Andrews T, Dao TP, Gomes T; participants in the 1st Human Cell Atlas Jamboree. EmptyDrops: distinguishing cells from empty droplets in droplet-based single-cell RNA sequencing data. Genome Biol 2019;20:63
19. Phipson B, Smyth GK. Permutation P-values should never be zero: calculating exact P-values when permutations are randomly drawn. Stat Appl Genet Mol Biol 2010;9:e39
20. Simes RJ. An improved Bonferroni procedure for multiple tests of significance. Biometrika 1986;73:751–754
21. Horn JL. A rationale and test for the number of factors in factor analysis. Psychometrika 1965;30:179–185
22. Jaccard P. The distribution of flora of the alpine zone. New Phytol 1912; 11:37–50
23. Blondel V, Guillaume J-L, Lambiotte R, Lefebvre E. Fast unfolding of communities in large networks. J Stat Mech 2008;2008:P10008
24. Stoeckius M, Zheng S, Houck-Loomis B, et al. Cell hashing with barcoded antibodies enables multiplexing and doublet detection for single cell genomics. Genome Biol 2018;19:224
25. Germain PL, Lun A, Garcia Meixide C, Macnair W, Robinson MD. Doublet identification in single-cell sequencing data using *scDblFinder*. F1000 Res 2021;10:979
26. Hafemeister C, Satija R. Normalization and variance stabilization of single-cell RNA-seq data using regularized negative binomial regression. Genome Biol 2019;20:296
27. Ekiz HA, Conley CJ, Stephens WZ, O'Connell RM. CIPR: a web-based R/shiny app and R package to annotate cell clusters in single cell RNA sequencing experiments. BMC Bioinformatics 2020;21:191
28. Robinson MD, Oshlack A. A scaling normalization method for differential expression analysis of RNA-seq data. Genome Biol 2010;11:R25
29. Robinson MD, McCarthy DJ, Smyth GK. edgeR: a Bioconductor package for differential expression analysis of digital gene expression data. Bioinformatics 2010;26:139–140
30. Hamaguchi K, Gaskins HR, Leiter EH. NIT-1, a pancreatic β-cell line established from a transgenic NOD/Lt mouse. Diabetes 1991;40:842–849
31. Zakharov PN, Hu H, Wan X, Unanue ER. Single-cell RNA sequencing of murine islets shows high cellular complexity at all stages of autoimmune diabetes. J Exp Med 2020;217:e20192362
32. Wculek SK, Heras-Murillo I, Mastrangelo A, et al. Oxidative phosphorylation selectively orchestrates tissue macrophage homeostasis. Immunity 2023;56: 516–530.e9
33. Tucker CG, Dwyer AJ, Fife BT, Martinov T. The role of programmed death-1 in type 1 diabetes. Curr Diab Rep 2021;21:20
34. Falcone M, Fousteri G. Role of the PD-1/PD-L1 dyad in the maintenance of pancreatic immune tolerance for prevention of type 1 diabetes. Front Endocrinol (Lausanne) 2020;11:569
35. Guleria I, Gubbels Bupp M, Dada S, et al. Mechanisms of PDL1-mediated regulation of autoimmune diabetes. Clin Immunol 2007;125:16–25
36. Osum KC, Burrack AL, Martinov T, et al. Interferon-gamma drives programmed death-ligand 1 expression on islet β cells to limit T cell function during autoimmune diabetes. Sci Rep 2018;8:8295
37. Sun C, Mezzadra R, Schumacher TN. Regulation and function of the PD-L1 checkpoint. Immunity 2018;48:434–452